EDGE ARTICLE

Highly conducting Wurster-type twisted covalent organic frameworks†

Julian M. Rotter,‡[a] Roman Guntermann, [ID] ‡[a] Michael Auth,[b] Andre Mähringer, [ID] [a] Andreas Sperlich, [ID] [b] Vladimir Dyakonov, [ID] [b] Dana D. Medina [ID] *[a] and Thomas Bein [ID] *[a]

Covalent organic frameworks (COFs) define a versatile structural paradigm combining attractive properties such as crystallinity, porosity, and chemical and structural modularity which are valuable for various applications. For the incorporation of COFs into optoelectronic devices, efficient charge carrier transport and intrinsic conductivity are often essential. Here, we report the synthesis of two imine-linked two-dimensional COFs, WTA and WBDT, featuring a redox-active Wurster-type motif based on the twisted tetragonal N,N,N',N'-tetraphenyl-1,4-phenylenediamine node. By condensing this unit with either terephthalaldehyde (TA) or benzodithiophene dialdehyde (BDT), COFs featuring a dual-pore kagome-type structure were obtained as highly crystalline materials with large specific surface areas and mesoporosity. In addition, the experimentally determined high conduction band energies of both COFs render them suitable candidates for oxidative doping. The incorporation of a benzodithiophene linear building block into the COF allows for high intrinsic macroscopic conductivity. Both anisotropic and average isotropic electrical conductivities were determined with van der Pauw measurements using oriented films and pressed pellets, respectively. Furthermore, the impact of different dopants such as F_4TCNQ, antimony pentachloride and iodine on the conductivities of the resulting doped COFs was studied. By using the strong organic acceptor F_4TCNQ, a massive increase of the radical cation density (up to 0.5 radicals per unit cell) and long-term stable electrical conductivity as high as 3.67 S m^{-1} were achieved for the anisotropic transport in an oriented film, one of the highest for any doped COF to date. Interestingly, no significant differences between isotropic and anisotropic charge transport were found in films and pressed pellets. This work expands the list of possible building nodes for electrically conducting COFs from planar systems to twisted geometries. The achievement of high and stable electrical conductivity paves the way for possible applications of new COFs in organic (opto)electronics.

1. Introduction

Covalent organic frameworks (COFs) have attracted great interest in materials science and polymer chemistry due to their highly modular construction principle and the resulting intriguing properties.[1] COFs emerge from condensation reactions of organic molecular building blocks, whereby the resulting covalent bonds form highly cross-linked porous frameworks.[2,3] They feature high crystallinity, high surface areas, and well-defined pore systems with pore sizes of up to several nm. By adhering to the principles of reticular synthesis, framework geometry and dimensionality, connectivity and porosity can be predetermined.[1] As a result of this modularity, various functionalities can be introduced into the framework through the design of the building block and stacking mode, thereby offering access to many different applications such as gas storage,[4,5] sensing,[6,7] catalysis,[8–10] charge storage,[11–13] or optoelectronics.[14–17] Besides the intrinsic structure of the building blocks, the type of linkage between them is of great significance. By varying the linkage, either electronically separated or highly conjugated systems can be designed.[2,18,19]

Recently, several two-dimensional (2D) COFs with enhanced electrical conductivity were reported.[20–22] A common feature of these frameworks is the cross-linking of the building blocks with either sp^2-hybridized carbon–carbon or carbon–nitrogen bonds. The π-conjugation of these linkages facilitates the through-bond charge transport by allowing for an increased charge delocalization, and therefore, in-plane conductivity is improved.[23] Another postulated design criterion for conducting

[a]*Department of Chemistry and Center for NanoScience (CeNS), Ludwig-Maximilians-Universität München, Butenandtstraße 5-13 (E), 81377 Munich, Germany. E-mail: bein@lmu.de; dmepc@cup.uni-muenchen.de*

[b]*Experimental Physics VI, Julius-Maximilians-Universität Würzburg, 97074 Würzburg, Germany*

† Electronic supplementary information (ESI) available. CCDC 2016924. For ESI and crystallographic data in CIF or other electronic format see DOI: 10.1039/d0sc03909h

‡ These authors contributed equally to this work.

COFs is the use of planar π-system geometries enabling extended π-orbital overlap between successive COF layers. Here, the enhanced π-system interactions are expected to facilitate the through-space charge transport perpendicular to the layers.[18,21] However, while various orientation-dependent studies of electrical conductivity have been carried out, there is no systematic investigation of isotropic *versus* anisotropic conductivity. The previously described two design strategies have been implemented for constructing 2D COF systems based on planar linkers such as pyrene,[10] tetrathiafulvalene,[22] phthalocyanine[21] or fully aromatic pyrazine systems.[24] In these cases, intrinsic conductivities ranging from 10^{-5} to 10^{-3} S m^{-1} were observed. Chemical doping of these systems with oxidants serving as guest-molecules in the pores led to a further increase in electrical conductivity. Notably, iodine so far appears to be the most suitable dopant, whereby the conductivity of the reported COFs was increased by two to three orders of magnitude.[22]

We recently reported on photoactive 2D COFs consisting of sterically demanding building blocks bearing significantly out-of-plane rotated phenyl groups such as in tetraphenylethylene. These types of COFs were shown to be suitable for transporting charge carriers in photoelectrochemical water splitting catalysis.[8,25] To expand the paradigm of non-planar, electrically conducting 2D COFs, additional features such as specific doping sites in sterically demanding linkers are of high interest. Here, we realize such a geometry with a Wurster-type motif, to obtain COFs based on *N,N,N′,N′*-tetraphenyl-1,4-phenylenediamine serving as a tetragonal node.

Wurster-type compounds are electron-rich molecules derived from *N,N,N′,N′*-tetramethyl-1,4-phenylenediamine (TMPD).[26] They can be easily oxidized, generating stabilized radical cations within their π-systems.[27] The doping of this motif through oxidation is well-studied, and the hereby generated radical cations show promising stability as conductive organic materials for charge transport or storage.[28–30] Organic salts based on TMPD as the electron donor and tetracyanoquinodimethane (TCNQ) as the electron acceptor show high electrical conductivity.[31]

Herein, we demonstrate that the Wurster motif can be embedded into different COFs, defined by using two different linear linker molecules. We also investigate the intrinsic conductivity of the two resulting Wurster-COFs. By condensing *N,N,N′,N′*-tetra(4-aminophenyl)benzene-1,4-diamine (**W**) with either terephthalaldehyde (TA) or the linear dialdehyde of benzodithiophene (BDT), conjugated, highly crystalline and porous imine-linked materials were obtained. We discuss the incorporation of the Wurster-type motif into a framework, structural aspects of the COFs, the resulting electronic properties, and study the effect of different dopants on the electrical conductivity of these novel frameworks.

2. Results and discussion

Synthesis

The Wurster-type COFs were synthesized under solvothermal conditions by condensing *N,N,N′,N′*-tetra(4-aminophenyl) benzene-1,4-diamine (**W**) with the linear aldehydes terephthalaldehyde (TA) or benzodithiophene dialdehyde (BDT) to form imine-linked COFs, namely WTA and WBDT (Fig. 1a). To this end, the respective building blocks were suspended in a mixture of mesitylene and benzyl alcohol and a catalytic amount of 6 M acetic acid was added to the mixture. The reaction vessel was sealed and heated for three days at 100 °C. Subsequently, the red precipitates were isolated by filtration and washed with the pure solvent mixture used in the reaction. The COFs were then purified using our recently reported supercritical CO$_2$ extraction protocol to remove residual guest molecules from the pores.[32]

Structural investigations

Powder X-ray diffraction (PXRD) analysis revealed the formation of highly crystalline materials with well-resolved reflections up to about 22° 2θ (Fig. 1b and c). To determine the framework topologies of the obtained COFs, several structural models for WTA and WBDT were developed. The combination of the tetragonal **W** building block with TA or BDT should either lead to a tetragonal topology or to a dual-pore, kagome-like topology.[33] Recent reports on tetragonal linkers with similar geometries, like tetraphenylethylene, have shown that kagome-type topologies are generally preferred.[33,34] Therefore, both structural models were simulated starting with an AA-type, eclipsed layer stacking arrangement, and the associated theoretical PXRD patterns were compared to the experimentally obtained ones. The simulations were carried out using the Forcite module of Materials Studio with the universal force field. Subsequently, the PXRD patterns of the simulated COFs were predicted using the reflex module. The simulations show that the dual-pore kagome structure model is in good agreement with the experimental patterns, and therefore we focused on this model for further modeling (Fig. 1b, c, S2 and S3†).

To refine the structure model of the COFs and to gain a deeper understanding of the geometric arrangement of the sterically demanding **W** unit within the framework, we synthesized a molecular fragment by condensing **W** with four monofunctional benzo[*b*]thiophene-2-carboxaldehyde units. Single crystal X-ray analysis of the resulting molecule revealed a counter-clockwise rotation of the triphenylamine moieties, resulting in a chair-like configuration of the molecular fragment (Fig. S1†). This building block configuration is different from the previously reported propeller-shaped geometries needed for kagome-type structures with hexagonal symmetry. Next, we constructed framework models of WTA and WBDT based on the hexagonal *P*6 space group, where the **W** linker adopts a propeller-like geometry, and the respective triclinic *P*1̄ symmetric frameworks, where the **W** configuration is adapted from the single-crystal data. All geometries were optimized using the density functional tight binding plus (DFTB+) code and the 3ob parameter set.[35–37] For both WTA and WBDT it was found that the *P*1̄ symmetry is indeed energetically favored by −27.9 or −31.2 kcal per cell, respectively, compared to the hexagonal kagome structures. We can conclude that an apparent kagome, dual-pore structure is present, namely a 2D
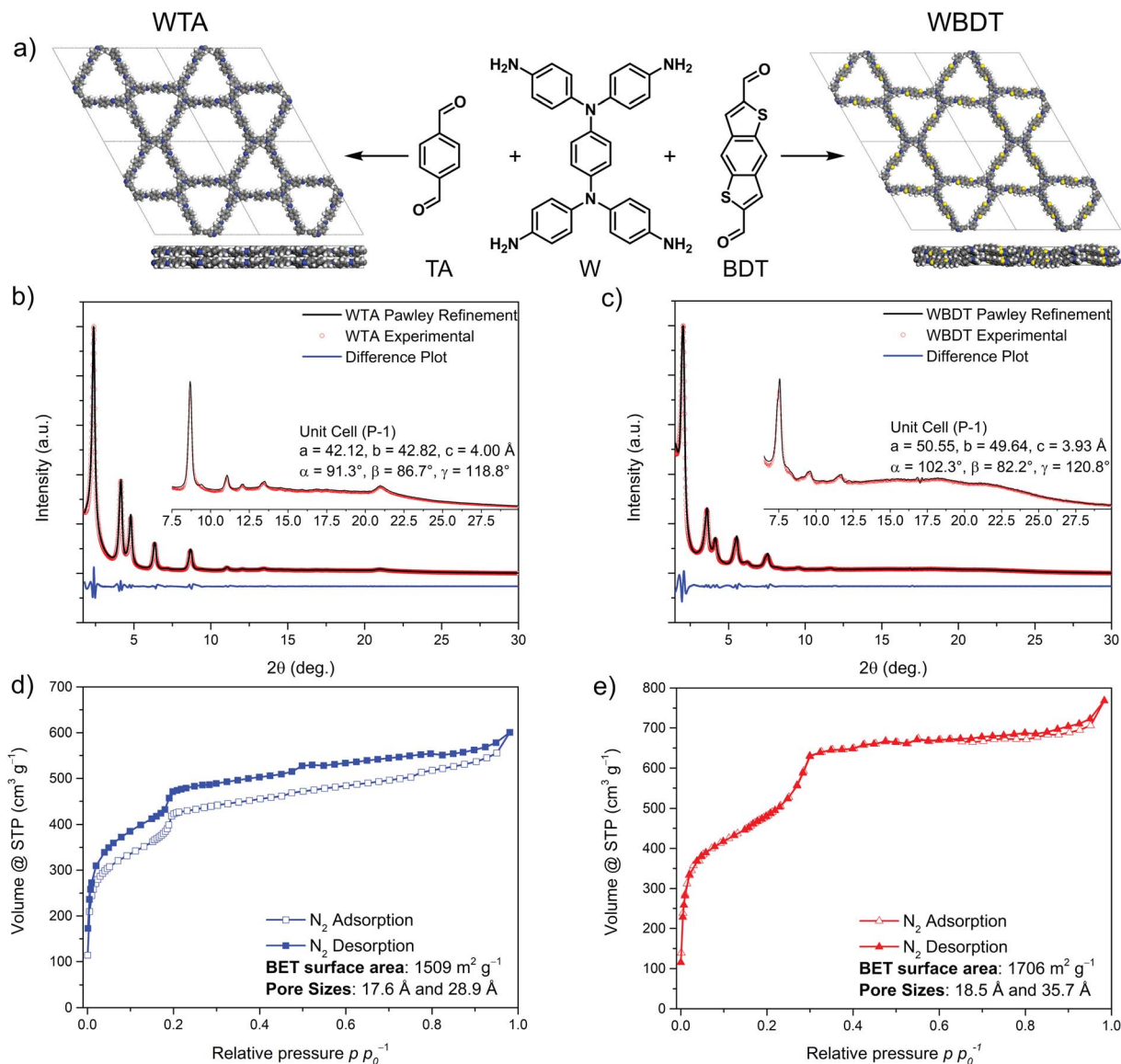
Fig. 1 (a) Schematic presentation of the synthesis of WTA and WBDT from the molecular building blocks. PXRD and Pawley refinement of WTA (b) and WBDT (c). Nitrogen physisorption isotherms of WTA (d) and WBDT (e).

trihexagonal tiling but only on a higher level of hierarchy, where the atoms are not arranged in hexagonal symmetry. On closer examination, this hexagonal symmetry condition is not preserved on the atomic level, and therefore, according to the symmetry constraints the structures can be only described as kagome-like.

Using the $P\bar{1}$ structures, the simulated unit cells were Pawley-refined to match with the experimental ones with very low fitting errors. Additionally, the diffraction patterns were indexed, and the reflections were attributed to *hkl* 100, 110, 200, 210, 300, 220, 310, 400, 500 and 001 (by order of appearance) for both COFs (the five strongest reflections for WTA and WBDT are at 2.378, 4.159, 4.795, 6.353, 8.675° 2θ and 2.039, 3.586, 4.137, 5.505, 7.547° 2θ, respectively). The observed (001) reflections are attributed to the π–π-stacking distances with *d*-spacing values of 4.00 Å and 3.93 Å for WTA and WBDT, respectively (Fig. 1b and c).

Porosity

To determine the internal surface area of the COFs, nitrogen physisorption isotherms were measured. Both COFs exhibit sorption isotherms featuring a mixture of type I and type IVb with two steep nitrogen uptake steps (Fig. 1d and e). Here, the first step, at low partial pressure, is characteristic for microporous materials, whereas the second step at higher relative partial pressures reveals additional capillary condensation, indicating the presence of mesopores. The calculated Brunauer, Emmett, Teller (BET) surface areas are 1509 m² g⁻¹ and 1706 m² g⁻¹ for WTA and WBDT, respectively. Pore sizes were calculated from the nitrogen isotherms using the quenched solid density functional theory (QSDFT) model for 1D cylindrical pores and carbon surfaces. For the COFs, two pore sizes were calculated with 1.76 nm and 2.89 nm (1.78 nm and 2.99 nm from structural simulations) for WTA and 1.79 nm and 3.51 nm (2.12 nm and

3.89 nm from structural simulations) for WBDT (Fig. S6 and S7†). Additionally, total pore volumes of 1.02 cm³ g⁻¹ and 1.17 cm³ g⁻¹ for WTA and WBDT were calculated, respectively. These results confirm the existence of a dual-pore system and strongly support the predicted structures and linker arrangements for WTA and WBDT.

COF morphology

The morphology of the obtained COFs was assessed by scanning electron microscopy (SEM). WTA powder consists of microparticles of a rosebud-like structure in which platelets intergrow to form larger spherical aggregates of about 2 to 3 μm (Fig. 2a). In contrast, WBDT powder consists of spherical particles of about 1 μm in size, which intergrow into larger connected structures (Fig. 2b). Transmission electron microscopy (TEM) clearly shows the polycrystalline nature of the two COFs. Domain sizes of about 200 nm and 100 nm can be observed for WTA and WBDT, respectively (Fig. 2c and d). In both cases, crystal domains where the c-zone axis is oriented parallel to the incident electron beam were detected. This visualises the pseudo-hexagonal pattern generated by the dual-pore arrangement, in good agreement with the PXRD and simulation data.

COF films

In addition to bulk synthesis, the surface growth of the Wurster-type COFs WTA and WBDT was investigated. In a typical thin film synthesis, a glass substrate was placed horizontally in the COF reaction vessel, and the COF powder synthesis procedure was carried out.[38] After 24 h, the substrate was recovered from the reaction vessel, and the respective COF was obtained as a transparent iridescent film on the bottom side of the substrate. To examine the crystallinity of the films, grazing incidence wide-angle X-ray scattering (GIWAXS) data were recorded using an incident angle of 0.22° and a 2D detector. For both COFs, strong X-ray reflections were observed, and the q-values of the respective signals match the ones from the bulk PXRD data (Fig. 3a and b) (WTA: q_y-values: 1.69, 2.98, 3.41, 4.55, 6.18 nm⁻¹; q_z-value: 15.7 nm⁻¹. WBDT: q_y-values: 1.44, 2.56, 2.90, 3.91, 4.42 nm⁻¹; q_z-value: 16.0 nm⁻¹). Furthermore, the low arching of the in-plane reflections at low q_y-values from about 2–8 nm⁻¹ and the out-of-plane π-stacking reflection at a larger q_z of about 16 nm⁻¹ reveal that the COFs grow as preferentially oriented film on the substrate, with many of the 1D pores positioned perpendicular to the substrate. SEM cross-sections of the films show thicknesses of about 80 nm for WTA and 210 nm for WBDT (Fig. 3c and e). Both materials grow as dense films without interstitial voids on the substrate. Additionally, thin platelet crystallites sized 100 to 200 nm emerge from the surface of the WTA film. The SEM top-view images reveal densely-packed films covering large areas without apparent cracks. For WTA, thin platelets are visible on the surface, while for WBDT, the film surface is composed of roughly spherical grains of about 50 nm in size (Fig. 3d and f).

Photophysical properties

The photophysical properties of the Wurster-type COF films were investigated by means of UV-vis absorption spectroscopy, photoluminescence (PL) and time-correlated single-photon counting (TCSPC) (Fig. 4a, S10 and S11†). Both COFs are red-colored materials and show similar light absorption
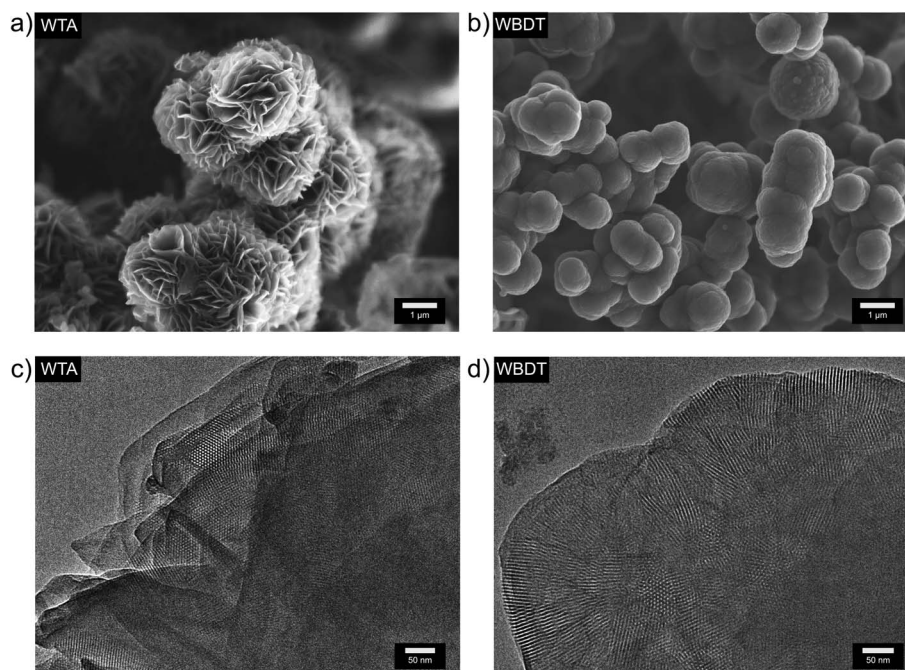
Fig. 2 (a) SEM image of WTA bulk material. (b) SEM image of WBDT bulk material. (c) TEM image of WTA bulk material. (d) TEM image of WBDT bulk material.
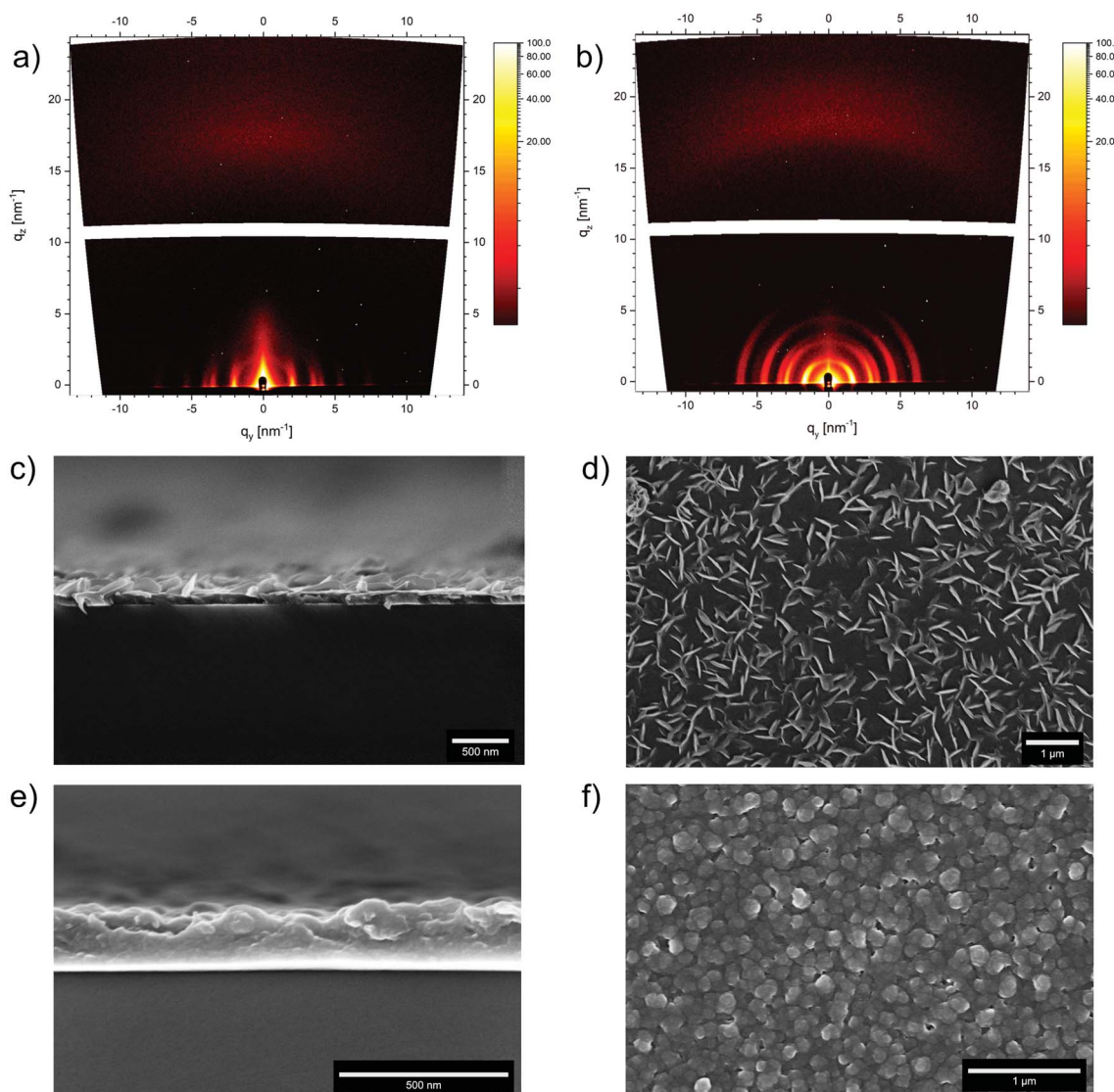
Fig. 3 GIWAXS 2D patterns of a WTA (a) and a WBDT (b) thin film on glass. (c) SEM cross-section image of a WTA thin film with (d), the corresponding top-view. (e) SEM cross-section of a WBDT thin film with (f), the corresponding top-view.

characteristics with a strong absorption in the visible spectrum. While WTA COF has an absorption onset at about 660 nm, the incorporation of the BDT building block into the COF causes a 40 nm red-shift (Fig. 4a). Assuming direct optical transitions for both materials, optical band gaps of 1.96 eV and 1.87 eV for WTA and WBDT COFs were calculated using Tauc plots (Fig. S8 and S9†). PL spectra of the COFs were recorded by exciting the materials with a 378 nm laser light source. The resulting spectra show large Stokes shifts of about 110 nm with PL emission maxima at 641 nm and 673 nm for WTA and WBDT, respectively, and overall broad emissions ranging from about 550 to 850 nm (Fig. 4a). Fluorescence lifetime decays were obtained by TCSPC using a 378 nm excitation wavelength. The decay curves were subsequently deconvoluted using the instrument response function (IRF) and a bi-exponential fit. TCSPC data were recorded at the respective PL maxima of the COFs under a nitrogen atmosphere. Here, very short lifetimes of the photoexcited

states can be observed. In WTA and WBDT, the major component, 82.7% and 86.4%, decays within 100 ps and 127 ps, respectively, while the minor component decays within 726 ps and 720 ps, respectively (Fig. S10 and S11†). These very short-lived excited states point to the presence of a push–pull system in the COF, in which electron-donating and -accepting motifs are separated. To probe whether such localization is present, we constructed theoretical model pore systems roughly the size of four unit cells for WTA (924 atoms) and WBDT (1032 atoms) using one layer of their refined structure models. Hydrogen atoms were used to terminate the lattice, and the hydrogen geometries were refined at the same DFTB+ (3ob) level while keeping the remainder of the structure restrained. Subsequently, orbital energies and localizations were calculated using density functional theory (DFT) at the PBE0-def2SVP level.[39] By plotting the localization of the highest occupied molecular orbitals (HOMOs) and lowest unoccupied molecular
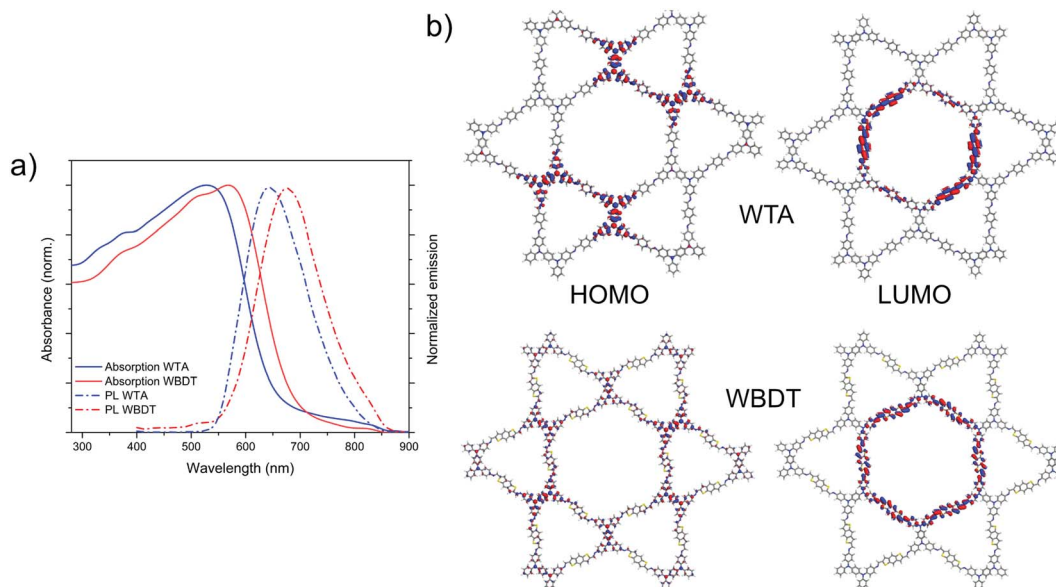
Fig. 4 (a) UV–vis absorption and PL emission spectra of WTA and WBDT thin films. (b) Waveplots of the frontier molecular orbital localizations for WTA and WBDT.

orbitals (LUMOs) for WTA and WBDT COFs, sharp spatial separations of the respective HOMOs and LUMOs can be observed. For both WTA and WBDT, the HOMO is strongly localized on the six central Wurster-type motifs while the LUMO spans along the inner linear linkers, which form the hexagonal pore (Fig. 4b). From these calculations, we can conclude that the electron-donating property of the Wurster-motif is preserved within the model systems. Consequently, we propose that the electron-donating- and -accepting parts are partially separated within the imine-linked frameworks, creating a push–pull system as indicated by the TCSPC data.

The retention of the electron-rich property of the Wurster-motif in the COFs should lead to valence band edges with high energies. Consequently, the COFs are expected to undergo oxidation at relatively low potentials. Here, we used cyclic voltammetry (CV) to determine the oxidation potentials of WTA and WBDT electrochemically. To this end, we grew the COFs as films on gold-coated glass substrates (modified with a 40 nm thick conductive gold coating). CV measurements of the respective films were subsequently carried out in a typical three-electrode setup using tetraethylammonium tetrafluoroborate as the electrolyte in argon-purged, anhydrous acetonitrile. The measurements were referenced against the ferrocene/ferrocenium (Fc/Fc^+) redox couple. For WTA, two redox couples were found at 0.82 V and 1.33 V $vs.$ Fc/Fc^+. Here, the narrow peak separations of 20 mV for the first and 62 mV for the second redox couple show that the oxidation of WTA is a highly reversible process and that the redox properties typical for Wurster-compounds are retained in the COF (Fig. 5a).[30]

WBDT shows two redox couples as well, the first at 0.62 V and the second at 0.97 V $vs.$ Fc/Fc^+. With oxidation-reduction peak separations of 170 mV for the first oxidation step and 220 mV for the second oxidation step, both oxidation steps can be described as quasi-reversible (Fig. 5b).

With the CV data at hand, the absolute energy of the valence band edge against the vacuum scale can be determined by comparing the oxidation onset potential against the HOMO energy of ferrocene.[40] Consequently, the energy of the conduction band edge can then be assessed by adding the optical band gap energy to the absolute energy of the valence band. The absolute valence band energy is determined by using the first oxidation onset potential and correlating this to the vacuum energy of the ferrocene HOMO energy at 4.8 eV.[40] Thereby, valence band energies of −5.2 eV and −5.0 eV and conduction band energies of −3.24 eV and −3.13 eV can be calculated for WTA and WBDT, respectively. The high conduction band energies of the COFs render the materials as suitable candidates for oxidative doping.

Electrical conductivity

Here, we measured the electrical conductivity of the materials presented as oriented films on glass, and as pressed pellets of bulk materials. The measurements were carried out using a van der Pauw four-probe setup with an electrode separation of 5 mm. For measurements of the different COFs, films with optimized crystallinity (but slightly different thickness) were employed. We note that for the van der Pauw analysis, film thickness is accounted for in the data evaluation. For WTA, electrical conductivities of 4.91×10^{-6} S m^{-1} for the pressed pellet and 3.78×10^{-6} S m^{-1} for the oriented film were determined. In contrast to WTA, the conductivity of WBDT is two to three orders of magnitude higher, with 2.70×10^{-4} S m^{-1} and 1.64×10^{-3} S m^{-1} for the pressed pellet and the oriented film, respectively. For WTA, no large difference in conductivity was measured for the oriented film and the pressed pellet. In the case of WBDT, the orientation of the film apparently increased the conductivity by one order of magnitude. We attribute this to the orientation of the crystallites in the film, where charge
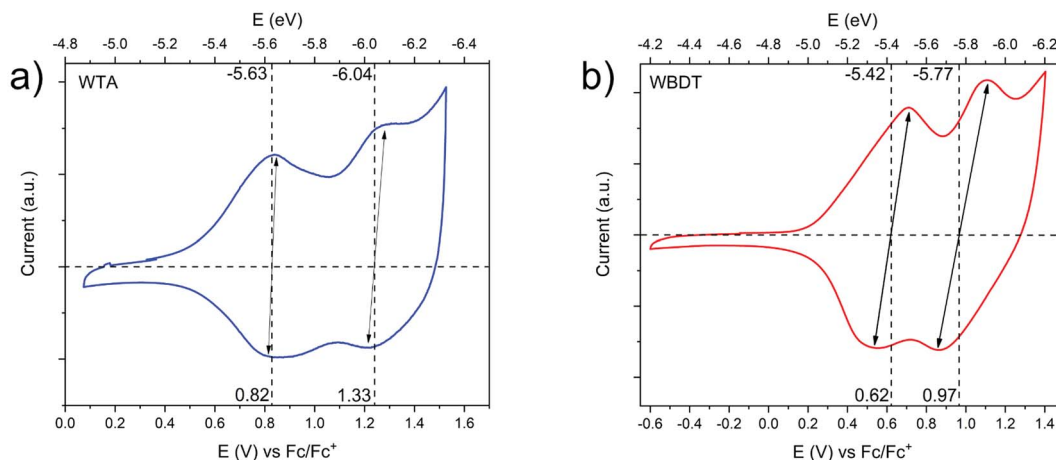
Fig. 5   Cyclic voltammograms of (a) WTA and (b) WBDT.

transport occurs mainly throughout the conjugated 2D layers. We attribute the absence of this effect for WTA to the film morphology, in which individual crystallites protrude from the plane of the oriented film and thus may act as barriers and impede charge transport.

COF doping

The measured intrinsic electrical conductivity values of WBDT are among the highest reported for COFs so far.[24] This fact is particularly remarkable since the WBDT COF layer geometry is twisted and non-planar, because highly planar 2D layers are viewed to be essential for effective charge trasnsport.[21] As Dinca and coworkers have previously reported, it is difficult to precisely compare measured electrical conductivities in molecular frameworks. In their analysis they show that the respective measurement methods have a great influence on the result and that conductivity values of different methods can often not be compared with each other.[41] Encouraged by the high intrinsic conductivities of the WBDT COF, we turned our attention to the chemical doping of the framework. As dopants, we chose 2,3,5,6-tetrafluoro-tetracyanoquinodimethane (F_4TCNQ) as an organic electron acceptor, antimony pentachloride ($SbCl_5$) as a strong inorganic oxidizer and iodine, which is commonly used for chemical doping of COFs.[24] Bulk WBDT was doped by adding the material to a solution consisting of acetonitrile and the dopant. As soon as the red COF powder contacted the doping solution, an instant color change to dark grey was observed, indicating a direct reaction, namely an electron transfer, between the material and the respective dopant. To ensure homogeneous doping of the framework, the material was stirred in the solution for one hour. The optimal dopant concentration was determined by using different amounts of F_4TCNQ and recording the resulting conductivities of pressed powder pellets. Thereby, a concentration of 0.3 equivalents of dopant, compared to the calculated number of Wurster-moieties, was determined as the ideal doping level, which was subsequently used for the doping experiments (Fig. S12†). Successful doping was observed with all three dopants, as illustrated by a strong

increase in conductivity. While doping with antimony pentachloride and iodine showed an increase in conductivity by two orders of magnitude to 3.09×10^{-2} S m^{-1} and 4.72×10^{-2} S m^{-1}, respectively, doping with F_4TCNQ proved to be even more effective, with an increase to 3.67 S m^{-1}. Thin films of WBDT were doped at a level similar to the bulk material by placing them into the solution of the respective dopant. For these experiments, comparable increases in conductivity were observed (see Table 1). In addition, bulk WTA was doped with F_4TCNQ to assess whether a similar increase in conductivity can also be observed. Here, the doping caused only a minor increase in conductivity from 4.91×10^{-6} S m^{-1} to 1.51×10^{-5} S m^{-1}. Therefore, we postulate that, although both COFs feature a Wurster-type motif, the efficiency of doping is also highly dependent on the linear building block. The integration of the electroactive BDT building block apparently facilitates charge transport, resulting in increased electrical conductivity and allowing for effective doping.

For a doping method to be meaningfully used for increasing conductivity, the resulting doping must be permanent and stable. While iodine has been successfully used to increase conductivities by several orders of magnitude for various COFs, the high vapor pressure of iodine hinders long-term doping and the measured conductivities decreased within 24 h after doping.[22] To assess the stability of the doping effect on the WBDT, we conducted time-dependent conductivity measurements of the respective pellets after 1 day, 3 days and 7 days

Table 1   Overview of the electrical conductivities measured for WTA and WBDT pressed pellets and thin films

COF system	Pressed pellet	Oriented film
WTA, pristine	4.91×10^{-6} S m^{-1}	3.78×10^{-6} S m^{-1}
WTA/F_4TCNQ	1.51×10^{-5} S m^{-1}	7.35×10^{-5} S m^{-1}
WBDT, pristine	2.70×10^{-4} S m^{-1}	1.64×10^{-3} S m^{-1}
WBDT/F_4TCNQ	3.67×10^{0} S m^{-1}	2.18×10^{0} S m^{-1}
WBDT/$SbCl_5$	3.09×10^{-2} S m^{-1}	6.86×10^{-2} S m^{-1}
WBDT/iodine	4.72×10^{-2} S m^{-1}	1.33×10^{-2} S m^{-1}

(Fig. 6a). Here, COFs doped with iodine and antimony pentachloride showed a decline of conductivity within the first 24 h after doping. Subsequently, the conductivity of the iodine-doped material stabilized at about one order of magnitude higher than the pristine COF pellet. In contrast to iodine, the conductivities of antimony pentachloride-doped WBDT continued to decline and fell below the values of the pristine COF pellet within 3 days. This effect is possibly caused by the highly corrosive nature of $SbCl_5$, which may result in local chemical defects in the COF structure without damaging the overall COF structure. Using the organic F_4TCNQ acceptor molecule proved to create doped COFs with stable conductivity over the whole course of the measurement (Fig. 6a), while also retaining the crystallinity of the COF (Fig. S13†). This result shows that a strong electron acceptor that does not chemically react with the host material is the ideal dopant to generate a highly conductive, stably doped COF.

To compare the efficiency of radical charge carrier generation, electron paramagnetic resonance (EPR) spectra were recorded for the doped and pristine WTA and WBDT bulk materials (Fig. 6b). For the pristine COFs, only minimal amounts of paramagnetic $WTA^{•+}$ and $WBDT^{•+}$ (in the range of 0.0025 radicals per unit cell) were found, which can be attributed to weakly doped as-synthesized COFs. The existence of a very small number of radicals within the pristine materials can be attributed to linker impurities or the oxidation of the COFs in air. The radical signal difference between the WTA pristine and WBDT pristine (about 10^{-3} radicals per unit cell) can be considered to be negligible. Upon doping WTA with F_4TCNQ, an increase by one order of magnitude in signal intensity can be observed. For the doping of WBDT, the signal intensity increases by three to four orders of magnitude for iodine and F_4TCNQ, respectively, while antimony pentachloride

doping is far less efficient. The signal intensity was quantified using a α,γ-bis-diphenylene-β-phenylallyl (BDPA) reference specimen resulting in 0.3–0.5 radicals per unit cell for the doped WBDT COF (eqn (S1)†). The observed relative EPR signal intensities are in direct correlation with the changes in the electrical conductivity recorded upon doping. Interestingly, two different species of $WBDT^{•+}$ radical centers are found in the EPR data. The pristine COF, as well as the antimony pentachloride- and F_4TCNQ-doped WBDT, feature a paramagnetic center at $g = 2.0044$, while the iodine-induced $WBDT^{•+}$ signal appears at $g = 2.005$ (Fig. 6b). This suggests that the doped species differ somewhat from each other, and that different $WBDT^{•+}$ radical populations are created. The spectra of the doped samples are featureless, Lorentzian-broadend lineshapes with no descernible hyperfine structure. This is indicative of strong delocalization, which is in agreement with the DFT calculations of HOMO/LUMO orbitals as shown in Fig. 4b.

As described above, the doping is not only reflected in the conductivity but also in a change of color. Therefore, UV-vis-NIR absorption spectra were recorded for the doped WBDT films. A strong bathochromic shift extends the absorption of all doped WBDT materials into the NIR up to 1500 nm (Fig. 6c). This red-shift is accompanied by significant bleaching in the visible range as compared to the pristine material. Upon doping, very broad absorption bands at around 700 nm emerge, which extend to 900 nm for iodine and F_4TCNQ and to more than 1000 nm for antimony pentachloride. This is in line with the observed immediate and strong color change for the COFs. The new absorption in the NIR is strongest for antimony pentachloride and weakest for F_4TCNQ. The resulting broad and low-intensity NIR absorption is typical for conjugated and doped COFs, where free radical charge carriers are delocalized and generate a mixed-valence state between doped and undoped
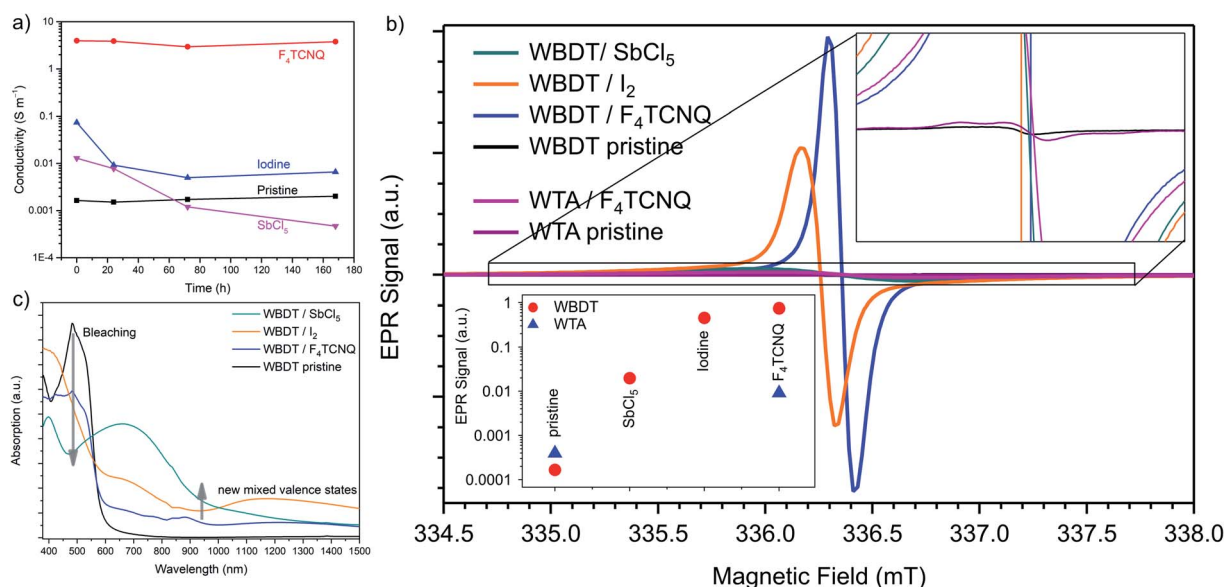

Fig. 6 (a) Time-dependent stability measurements of the conductivity of WBDT with different dopings. (b) EPR spectra of WTA, WBDT and the respective dopings. The insets show a zoom for the undoped spectra and the relative EPR signal intensities. (c) UV-vis-NIR absorption spectra of doped WBDT.

sites which can be related to the enhanced electrical conductivity.[22]

3. Conclusion

We report two novel, 2D imine-linked COFs based on the electron-rich Wurster-motif, named WTA and WBDT. The highly crystalline materials were analyzed by PXRD refinement and structure modeling. Nitrogen physisorption revealed the existence of dual-pore systems with high surface areas. Additionally, oriented thin films of the COFs were synthesized, which were subsequently used to study the optical properties and electronic energy levels. The macroscopic electrical conductivity of the COFs was studied by means of van der Pauw measurements on pressed pellets and oriented thin films grown on glass substrates. Depending on the linear linker in the COF, conductivities of the pristine materials as high as 1.64×10^{-3} S m^{-1} were determined. Furthermore, different dopants as well as different doping concentrations were investigated to create the radical cation forms of the COFs, and their long-term effect on the electrical conductivity was assessed. The use of F$_4$TCNQ as a strong electron acceptor yielded conductivities as high as 3.67 S m^{-1}, one of the highest values for doped imine-linked COFs reported so far. Moreover, the impact of doping on the optical absorption and the formation of radicals in the COF could be correlated with the changes in conductivity. In contrast to previous work in the field of conductive COFs. In addition, it was shown that the high conductivities resulting from doping are stable over time for the organic acceptor molecule F$_4$TCNQ. This stability is of central importance in order to be able to exploit high conductivities by doping permanently.

In the context of electrical conductivity, we discovered that the geometry of the linker can deviate from planarity and still lead to high conductivity values. Moreover, these non-planar COFs have the added value of high crystallinity and robustness achieved through molecular docking sites provided by the Wurster node. Encoding electrical conductivity in these non-planar systems requires the selection of electroactive building blocks. Increasing the electrical conductivity in these systems through doping is highly dependent on the dopant, and we attribute the long-term stability to a combination of factors such as a robust framework and a chemically innocent dopant with low vapor pressure. We anticipate that these results will contribute to the development of new strategies for the design of COFs for various (opto)electronic applications.

Conflicts of interest

There are no conflicts to declare.

Acknowledgements

References

1 C. S. Diercks and O. M. Yaghi, The atom, the molecule, and the covalent organic framework, *Science*, 2017, **355**, eaal1585.

2 M. S. Lohse and T. Bein, Covalent Organic Frameworks: Structures, Synthesis, and Applications, *Adv. Funct. Mater.*, 2018, **355**, 1705553.

3 N. Huang, P. Wang and D. Jiang, Covalent organic frameworks: a materials platform for structural and functional designs, *Nat. Rev. Mater.*, 2016, **1**, 1–19.

4 H. Fan, A. Mundstock, A. Feldhoff, A. Knebel, J. Gu, H. Meng and J. Caro, Covalent Organic Framework-Covalent Organic Framework Bilayer Membranes for Highly Selective Gas Separation, *J. Am. Chem. Soc.*, 2018, **140**, 10094–10098.

5 Z. Li, X. Feng, Y. Zou, Y. Zhang, H. Xia, X. Liu and Y. Mu, A 2D azine-linked covalent organic framework for gas storage applications, *Chem. Commun.*, 2014, **50**, 13825–13828.

6 S.-Y. Ding, M. Dong, Y.-W. Wang, Y.-T. Chen, H.-Z. Wang, C.-Y. Su and W. Wang, Thioether-Based Fluorescent Covalent Organic Framework for Selective Detection and Facile Removal of Mercury(II), *J. Am. Chem. Soc.*, 2016, **138**, 3031–3037.

7 Z. Li, Y. Zhang, H. Xia, Y. Mu and X. Liu, A robust and luminescent covalent organic framework as a highly sensitive and selective sensor for the detection of Cu^{2+} ions, *Chem. Commun.*, 2016, **52**, 6613–6616.

8 T. Sick, A. G. Hufnagel, J. Kampmann, I. Kondofersky, M. Calik, J. M. Rotter, A. Evans, M. Döblinger, S. Herbert, K. Peters, *et al.*, Oriented Films of Conjugated 2D Covalent Organic Frameworks as Photocathodes for Water Splitting, *J. Am. Chem. Soc.*, 2018, **140**, 2085–2092.

9 X. Wang, L. Chen, S. Y. Chong, M. A. Little, Y. Wu, W.-H. Zhu, R. Clowes, Y. Yan, M. A. Zwijnenburg, R. S. Sprick, *et al.*, Sulfone-containing covalent organic frameworks for photocatalytic hydrogen evolution from water, *Nat. Chem.*, 2018, **10**, 1180–1189.

10 E. Jin, Z. Lan, Q. Jiang, K. Geng, G. Li, X. Wang and D. Jiang, 2D sp^2 Carbon-Conjugated Covalent Organic Frameworks for Photocatalytic Hydrogen Production from Water, *Chem*, 2019, **5**, 1632–1647.

11 C. R. DeBlase, K. E. Silberstein, T.-T. Truong, H. D. Abruña and W. R. Dichtel, β-Ketoenamine-linked covalent organic frameworks capable of pseudocapacitive energy storage, *J. Am. Chem. Soc.*, 2013, **135**, 16821–16824.

12 S. Chandra, D. Roy Chowdhury, M. Addicoat, T. Heine, A. Paul and R. Banerjee, Molecular Level Control of the Capacitance of Two-Dimensional Covalent Organic Frameworks: Role of Hydrogen Bonding in Energy Storage Materials, *Chem. Mater.*, 2017, **29**, 2074–2080.

13 A. Halder, M. Ghosh, M. A. Khayum, S. Bera, M. Addicoat, H. S. Sasmal, S. Karak, S. Kurungot and R. Banerjee, Interlayer Hydrogen-Bonded Covalent Organic Frameworks as High-Performance Supercapacitors, *J. Am. Chem. Soc.*, 2018, **140**, 10941–10945.

14 H. Wang, Z. Zeng, P. Xu, L. Li, G. Zeng, R. Xiao, Z. Tang, D. Huang, L. Tang, C. Lai, *et al.*, Recent progress in covalent organic framework thin films: fabrications, applications and perspectives, *Chem. Soc. Rev.*, 2019, **48**, 488–516.

15 D. D. Medina, M. L. Petrus, A. N. Jumabekov, J. T. Margraf, S. Weinberger, J. M. Rotter, T. Clark and T. Bein, Directional Charge-Carrier Transport in Oriented Benzodithiophene Covalent Organic Framework Thin Films, *ACS Nano*, 2017, **11**, 2706–2713.

16 D. D. Medina, V. Werner, F. Auras, R. Tautz, M. Dogru, J. Schuster, S. Linke, M. Döblinger, J. Feldmann, P. Knochel, *et al.*, Oriented thin films of a benzodithiophene covalent organic framework, *ACS Nano*, 2014, **8**, 4042–4052.

17 D. D. Medina, T. Sick and T. Bein, Photoactive and Conducting Covalent Organic Frameworks, *Adv. Energy Mater.*, 2017, **7**, 1700387.

18 J. Guo, Y. Xu, S. Jin, L. Chen, T. Kaji, Y. Honsho, M. A. Addicoat, J. Kim, A. Saeki, H. Ihee, *et al.*, Conjugated organic framework with three-dimensionally ordered stable structure and delocalized π clouds, *Nat. Commun.*, 2013, **4**, 2736.

19 M. Calik, F. Auras, L. M. Salonen, K. Bader, I. Grill, M. Handloser, D. D. Medina, M. Dogru, F. Löbermann, D. Trauner, *et al.*, Extraction of photogenerated electrons and holes from a covalent organic framework integrated heterojunction, *J. Am. Chem. Soc.*, 2014, **136**, 17802–17807.

20 H. Li, J. Chang, S. Li, X. Guan, D. Li, C. Li, L. Tang, M. Xue, Y. Yan, V. Valtchev, *et al.*, Three-Dimensional Tetrathiafulvalene-Based Covalent Organic Frameworks for Tunable Electrical Conductivity, *J. Am. Chem. Soc.*, 2019, **141**, 13324–13329.

21 Z. Meng, R. M. Stolz and K. A. Mirica, Two-Dimensional Chemiresistive Covalent Organic Framework with High Intrinsic Conductivity, *J. Am. Chem. Soc.*, 2019, **141**, 11929–11937.

22 S.-L. Cai, Y.-B. Zhang, A. B. Pun, B. He, J. Yang, F. M. Toma, I. D. Sharp, O. M. Yaghi, J. Fan, S.-R. Zheng, *et al.*, Tunable electrical conductivity in oriented thin films of tetrathiafulvalene-based covalent organic framework, *Chem. Sci.*, 2014, **5**, 4693–4700.

23 C. R. DeBlase and W. R. Dichtel, Moving Beyond Boron: The Emergence of New Linkage Chemistries in Covalent Organic Frameworks, *Macromolecules*, 2016, **49**, 5297–5305.

24 S. Kim and H. C. Choi, Light-promoted synthesis of highly-conjugated crystalline covalent organic framework, *Commun. Chem.*, 2019, **2**, 1–8.

25 J. M. Rotter, S. Weinberger, J. Kampmann, T. Sick, M. Shalom, T. Bein and D. D. Medina, Covalent Organic Framework Films through Electrophoretic Deposition—

26 Y. Yamashita and M. Tomura, Highly polarized electron donors, acceptors and donor–acceptor compounds for organic conductors, *J. Mater. Chem.*, 1998, **8**, 1933–1944.

27 J. Zhang, S.-Z. Guo, Y.-B. Dong, L. Rao, J. Yin, G.-A. Yu, F. Hartl and S. H. Liu, Multistep Oxidation of Diethynyl Oligophenylamine-Bridged Diruthenium and Diiron Complexes, *Inorg. Chem.*, 2017, **56**, 1001–1015.

28 P. S. Ghalsasi, B. Cage and J. L. Yarger, Studies on TMPD:TCNB; a donor–acceptor with room temperature paramagnetism and n-pi interaction, *Molecules*, 2004, **9**, 808–814.

29 C. -J. Chen, H. -J. Yen, W. -C. Chen and G. -S. Liou, Novel high-performance polymer memory devices containing (OMe)₂tetraphenyl-*p*-phenylenediamine moieties, *J. Polym. Sci., Part A: Polym. Chem.*, 2011, **49**, 3709–3718.

30 A. F. M. EL-Mahdy, M. G. Mohamed, T. H. Mansoure, H.-H. Yu, T. Chen and S.-W. Kuo, Ultrastable tetraphenyl-p-phenylenediamine-based covalent organic frameworks as platforms for high-performance electrochemical supercapacitors, *Chem. Commun.*, 2019, **55**, 14890–14893.

31 H. A. Staab, R. Hinz, G. H. Knaus and C. Krieger, Elektron-Donor-Acceptor-Verbindungen, XXXII. Ein Elektron-Donor-Acceptor-Paracyclophan mit N,N,N′,N′-Tetramethyl-p-phenylendiamin- und 7,7,8,8-Tetracyanchinodimethan-Untereinheiten, *Chem. Ber.*, 1983, **116**, 2835–2847.

32 T. Sick, J. M. Rotter, S. Reuter, S. Kandambeth, N. N. Bach, M. Döblinger, J. Merz, T. Clark, T. B. Marder, T. Bein, *et al.*, Switching On and Off Interlayer Correlations and Porosity in 2D Covalent Organic Frameworks, *J. Am. Chem. Soc.*, 2019, **141**, 12570–12581.

33 L. Ascherl, T. Sick, J. T. Margraf, S. H. Lapidus, M. Calik, C. Hettstedt, K. Karaghiosoff, M. Döblinger, T. Clark, K. W. Chapman, *et al.*, Molecular docking sites designed for the generation of highly crystalline covalent organic frameworks, *Nat. Chem.*, 2016, **8**, 310–316.

34 S. Dalapati, E. Jin, M. Addicoat, T. Heine and D. Jiang, Highly Emissive Covalent Organic Frameworks, *J. Am. Chem. Soc.*, 2016, **138**, 5797–5800.

35 B. Aradi, B. Hourahine and T. Frauenheim, DFTB+, a sparse matrix-based implementation of the DFTB method, *J. Phys. Chem. A*, 2007, **111**, 5678–5684.

36 M. Gaus, A. Goez and M. Elstner, Parametrization and Benchmark of DFTB3 for Organic Molecules, *J. Theor. Comput. Chem.*, 2013, **9**, 338–354.

37 M. Gaus, X. Lu, M. Elstner and Q. Cui, Parameterization of DFTB3/3OB for Sulfur and Phosphorus for Chemical and Biological Applications, *J. Theor. Comput. Chem.*, 2014, **10**, 1518–1537.

38 S. Wuttke, D. D. Medina, J. M. Rotter, S. Begum, T. Stassin, R. Ameloot, M. Oschatz and M. Tsotsalas, Bringing Porous Organic and Carbon-Based Materials toward Thin-Film Applications, *Adv. Funct. Mater.*, 2018, **28**, 1801545.

39 B. P. Biswal, H. A. Vignolo-González, T. Banerjee, L. Grunenberg, G. Savasci, K. Gottschling, J. Nuss, C. Ochsenfeld and B. V. Lotsch, Sustained Solar H₂

Evolution from a Thiazolo5,4-dthiazole-Bridged Covalent Organic Framework and Nickel-Thiolate Cluster in Water, *J. Am. Chem. Soc.*, 2019, **141**, 11082–11092.

40 C. M. Cardona, W. Li, A. E. Kaifer, D. Stockdale and G. C. Bazan, Electrochemical considerations for determining absolute frontier orbital energy levels of conjugated polymers for solar cell applications, *Adv. Mater.*, 2011, **23**, 2367–2371.

41 L. Sun, S. S. Park, D. Sheberla and M. Dincă, Measuring and Reporting Electrical Conductivity in Metal-Organic Frameworks: Cd_2(TTFTB) as a Case Study, *J. Am. Chem. Soc.*, 2016, **138**, 14772–14782.